Biomaterials in repairing rat femoral defects: in vivo insights from small animal positron emission tomography/computed tomography (PET/CT) studies

Neuber, C.; Schulze, S.; Förster, Y.; Hofheinz, F.; Wodke, J.; Möller, S.; Schnabelrauch, M.; Hintze, V.; Scharnweber, D.; Rammelt, S.; Pietzsch, J.;

Originally published:

November 2019

Clinical Hemorheology and Microcirculation 73(2019), 177-194

DOI: https://doi.org/10.3233/CH-199208

Biomaterials in repairing rat femoral defects: *In vivo* insights from small animal positron emission tomography/computed tomography (PET/CT) studies

Christin Neuber[a], Sabine Schulze[b,c], Yvonne Förster[b,c], Frank Hofheinz[d], Johanna Wodke[a], Stephanie Möller[e], Matthias Schnabelrauch[e], Vera Hintze[f], Dieter Scharnweber[f,g], Stefan Rammelt[b,c,g] and Jens Pietzsch[a,h,*]

[a]*Helmholtz-Zentrum Dresden-Rossendorf, Institute of Radiopharmaceutical Cancer Research, Department Radiopharmaceutical and Chemical Biology, Dresden, Germany*
[b]*Technische Universität Dresden, University Hospital Carl Gustav Carus, University Center for Orthopaedics and Traumatology, Dresden, Germany*
[c]*Technische Universität Dresden, Faculty of Medicine, Centre for Translational Bone, Joint and Soft Tissue Research, Dresden, Germany*
[d]*Helmholtz-Zentrum Dresden-Rossendorf, Institute of Radiopharmaceutical Cancer Research, Department Positron Emission Tomography, Dresden, Germany*
[e]*Biomaterials Department, INNOVENT e.V., Jena, Germany*
[f]*Technische Universität Dresden, Max Bergmann Center of Biomaterials, Institute of Materials Science, Dresden, Germany*
[g]*Center of Regenerative Therapies Dresden (CRTD), Dresden, Germany*
[h]*Technische Universität Dresden, School of Science, Faculty of Chemistry and Food Chemistry, Dresden, Germany*

Abstract. Biomaterials coated with artificial extracellular matrices (aECM) are intended to support the healing of critical size bone defects. This pilot study investigated (i) the feasibility of dual-tracer PET/CT imaging for functional characterization of biomaterial-assisted bone healing in a rat femoral defect model and (ii) the bone healing ability of polycaprolactone-*co*-lactide (PCL) scaffolds, coated with various aECM consisting of collagen type I (Col) and glycosaminoglycans (GAGs) such as chondroitin sulfate (CS) or polysulfated hyaluronan (sHA3). [^{18}F]FDG and [^{18}F]fluoride PET 4 and 8 weeks after implantation of aECM-coated PCL scaffolds, which provide an *in vivo* measure of cellular activation and bone mineralization, respectively, combined with CT imaging (*in vivo/ex vivo*) and histological/immunohistochemical investigations (*ex vivo*) showed that coating with CS in particular is beneficial for bone healing. The possible involvement of COX-2 and TGase 2, key enzymes of inflammation and ECM remodeling, in these processes offers starting points for targeted adjuvant therapy in the course of various bone healing phases. Our investigations show the feasibility of the selected dual-tracer approach for PET/CT imaging. In principle, this approach can be extended by further PET tracers for the functional characterization of physiological processes such as hypoxia/reperfusion or selected molecular players.

Keywords: Artificial extracellular matrices, bone healing, [^{18}F]fluorodeoxyglucose, [^{18}F]fluoride, glycosaminoglycans, inflammation, metabolism, molecular imaging, revascularization

*Corresponding author: Prof. Jens Pietzsch, Helmholtz-Zentrum Dresden-Rossendorf, Institute of Radiopharmaceutical Cancer Research, Department Radiopharmaceutical and Chemical Biology, Bautzner Landstrasse 400, 01328 Dresden, Germany. E-mail: j.pietzsch@hzdr.de.

1. Introduction

Critical size bone defects are still one of the most challenging conditions to treat in clinical orthopedics. They arise from trauma, but can also result from loss or resection of bone as a consequence of infections, primary tumors, or metastases [1]. The management of critical size bone defects significantly deteriorates if comorbidities like diabetes or osteoporosis are present [2], a situation getting more prominent in face of our ageing society. Currently, autologous bone grafting is still the gold standard for treatment of large bone defects, despite of limited availability, significant donor site morbidity, and the need of an additional surgery [3, 4]. To overcome the drawbacks of autografts, and also of allografts, a broad spectrum of biomaterials has been developed during the last years [1]. To be beneficial for bone formation, a suitable biomaterial has to provide an osteoconductive structure and, moreover, should be osteoinductive and osteogenic [5].

Smart biomaterials should exploit the endogenous bone healing capacity by mimicking the biology of bone healing [1]. Glycosaminoglycans (GAGs) like chondroitin sulfate (CS) and hyaluronan (HA) are important multifunctional components of the extracellular matrix (ECM) in bone and, thereby, may stimulate bone healing by recruitment of mesenchymal stromal cells and by supporting their osteogenic differentiation [6–9]. Therefore, coating of bone implants with artificial ECM (aECM) components appears to be one promising approach to enhance bone healing [10–12]. Using aECM-coated polymer (titanium-coated polyetheretherketone, Ti-PEEK) plates it became evident that new bone formation took place mainly from the bone defect margins using the Ti-PEEK plate as a guide [13]. To allow ingrowth of new bone with the aim of a complete regeneration of the critical size bone defect, biodegradable, three-dimensional, embroidered polycaprolactone-*co*-lactide (PCL) scaffolds, coated again with aECM components, were developed [13–16]. Previous studies could already confirm improvement of bone healing, especially by a combination of collagen type I (Col), the most abundant organic matrix component in bone, and CS. However, using *ex vivo* radiography, μCT, and histological investigations the previous studies were limited to pre-defined endpoints and did not allow for intra-individual follow-up.

Functional molecular imaging by positron emission tomography (PET) or single-photon emission computed tomography (SPECT), in combination with morphological imaging by computed tomography (CT) or magnetic resonance imaging (MRI) is a very powerful tool to follow biomaterial-assisted bone healing *in vivo*. By using several PET or SPECT tracers, it is possible not only to measure the course of physiological processes, such as metabolic activation of cells, bone formation, inflammation, hypoxia, vascularisation, or the development of infections, but also to investigate the functional expression of selected molecular targets, such as receptors, transporters, or enzymes [17–19]. In this regard, as one example, Cheng et al. recently demonstrated the use of [^{18}F]fluoride PET/CT to follow the influence of different multifunctional biodegradable implants on bone healing in an experimental rat model of osteoporotic fractures [20, 21].

The present pilot study demonstrated the feasibility of dual-tracer PET/CT imaging, using 2-[^{18}F]fluoro-2-deoxy-D-glucose ([^{18}F]FDG) and [^{18}F]fluoride, for the intra-individual, functional characterization of biomaterial-assisted bone healing in a rat critical size femur defect model. Implantation of porous, biodegradable PCL scaffolds coated with aECM consisting of Col and GAGs promotes bone healing by providing a temporary matrix for bone regeneration and also eliminates the need for a second operation to remove the implant as degradation occurs simultaneously.

2. Material and methods

2.1. Preparation of aECM coating solutions

Chondroitin sulfate (CS; Kraeber GmbH, Ellerbek, Germany; degree of sufation (DS) 0.8; weight-average molecular weight (Mw) 22 kDa; from bovine trachea; mixture of chondroitin-4-sulfate and

chondroitin-6-sulfate (70/30)) was purified by dialysis [13]. Low molecular weight hyaluronan (HA, Mw 57 kDa) was prepared by ozonolysis starting from high molecular weight native hyaluronic acid (Aqua Biochem Dessau, Mw 1.000 kDa) as previously described [22, 23]. The reaction time for ozonolysis was one hour. The polysulfated hyaluronan derivative (sHA3; DS 3.0; Mw 53 kDa) was synthesized by sulfation of high molecular weight HA with SO_3-DMF and characterized as previously reported [24, 25]. For sHA3 synthesis, the ratio of OH/SO_3 was 1:20.

Preparation of artificial extracellular matrices (aECM) was performed as described elsewhere [13]. In brief, for 'Col' group, a Col stock solution (rat tail tendon collagen type I, BD Bioscience, Heidelberg, Germany) was diluted to 2 mg/ml with ice-cold 10 mM acetic acid and mixed with an equal volume of 60 mM ice-cold phosphate buffer (50 mM disodium hydrogen phosphate and 10 mM potassium dihydrogen phosphate, pH 7.4). For 'CS' and 'sHA3' group, Col stock solution was mixed with an equal volume of CS (2.53 mg/ml) and sHA3 (3.92 mg/ml), respectively, with an equal molarity of 5 mM disaccharide units each, dissolved in the same ice-cold phosphate buffer. These coating solutions were used for coating of PCL scaffolds.

2.2. Preparation of PCL scaffolds and coating with aECM

Polycaprolactone-*co*-lactide (PCL) scaffolds were prepared as described elsewhere [14, 15]. In brief, the copolymer of L-lactide and ε-caprolactone (75/25) was melt spun and resulted in a synthetic, resorbable, monofilament fiber, available as PCL suture (Catgut, Markneukirchen, Germany). The textile PCL scaffolds were made on a computer aided embroidery machine and had a diameter of 5 mm.

For immobilization of aECM on the PCL scaffolds, four scaffolds each were placed in a 24-well tissue culture plate and incubated with 400 µl of the respective coating solutions. *In vitro* fibrillogenesis of Col proceeded for 16–18 h at 37°C. Afterwards, the scaffolds were removed from the fibrillogenesis solution, frozen for 2 hours at –80°C and, then, freeze-dried overnight. This was followed by two brief washing steps in deionized water and a drying step under laminar flow for 30 min. Afterwards the scaffolds were frozen for 2 hours at –80°C and freeze-dried again.

Five aECM-coated PCL scaffolds were piled up on top of each other, fixed with a PCL suture, and were sterilized by gamma irradiation using 15 kGy (BBF Sterilisationsservice, Kernen, Germany).

2.3. Animal surgery

All animal experiments were carried out according to the guidelines of the German Regulations for Animal Welfare. The protocols were approved by the local Ethical Committee for Animal Experiments (AZ 24–9168.11–1/2013–40). Male Wistar rats with an average body weight of 300 g were obtained from Janvier Inc. (Le Genest Saint Isle, France). All animals were housed according to the European guidelines for the care and use of laboratory animals with a 12/12 h light/dark cycle and free access to food and water.

Rats were anesthetized by intraperitoneal injection of a solution of ketamine (100 mg/kg body weight; Riemser Arzneimittel, Greifswald, Germany) and xylazine (10 mg/kg body weight; Pharma-Partner, Hamburg, Germany). Surgery was performed as described elsewhere by us with some modifications [13] and is shown in Fig. 1A. In brief, the right femur was surgically exposed and a 5-hole plate was fixed with 4 screws at the femur. The 5-hole plate (made out of a 1.5 plate with 12 holes) and the screws (1.5 mm × 6 mm, cortex screw) were available from Synthes (Umkirch, Germany). A 5 mm critical size bone defect was created at the femur midshaft using a wire saw. The rats were randomly divided into 4 groups: (1) negative control ('NC') where the defect was left empty and 3 groups where a PCL scaffold coated with (2) collagen type I ('Col'), (3) Col plus CS ('CS'), or (4) Col plus sHA3

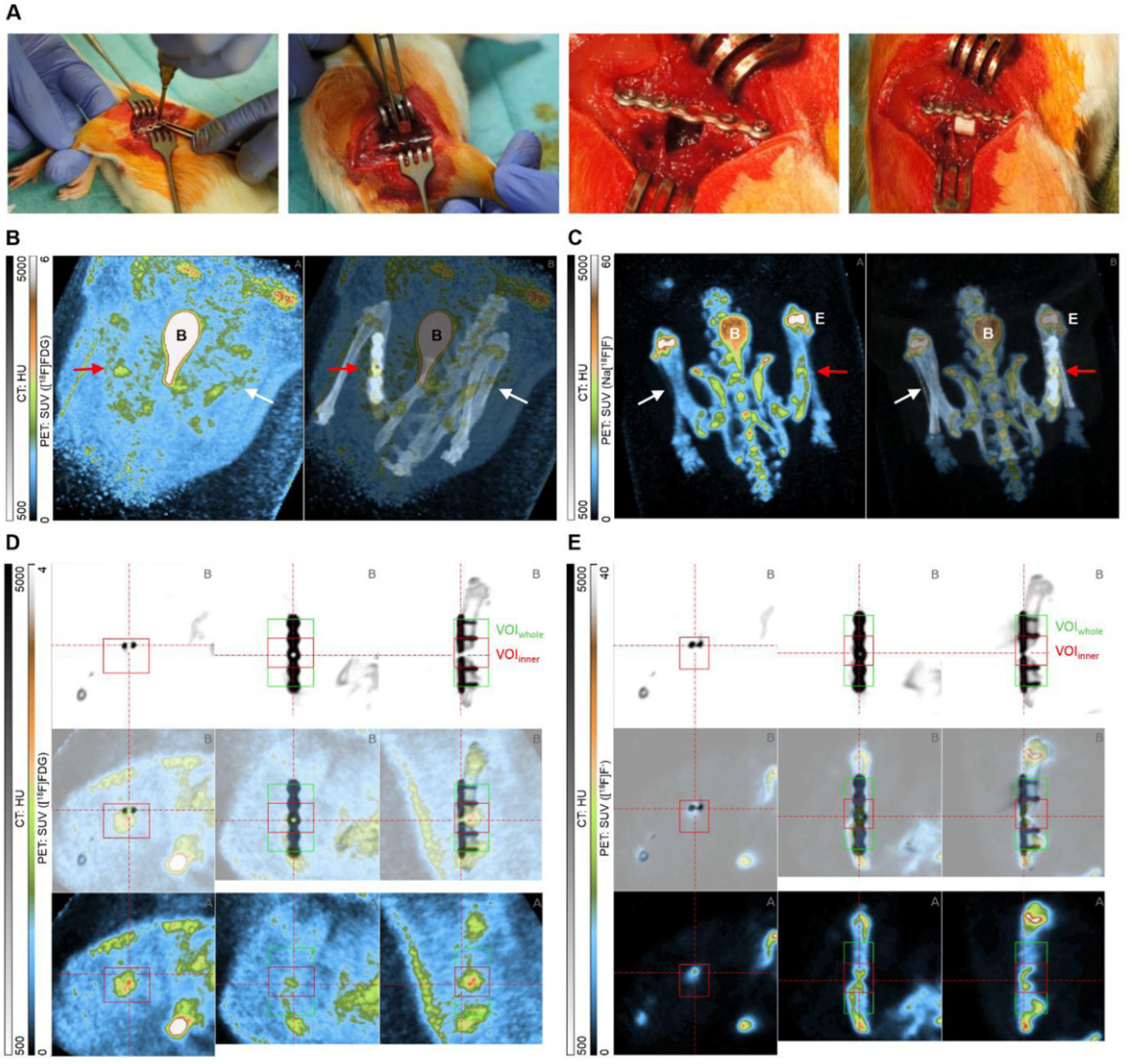

Fig. 1. (A) Surgery of a rat resulting in a 5 mm critical size bone defect at the right femur. (B–E) Representative PET/CT images of a rat (pelvic region) after i.v. injection of [^{18}F]FDG (left panel) and [^{18}F]fluoride (right panel). (B/C) Rotated maximum intensity projection (MIP) of PET data (each left) fused to CT image (each right). B – bladder, E - epiphysis (D/E) Two-dimensional view of femur defect fixed by 5-hole plate and 4 screws visualized by CT (upper panel), PET (lower panel), and fused PET/CT image (mid panel).

('sHA3') was press-fit inserted into the defect. The wound was closed and the animals were allowed to walk free immediately. For postoperative analgesia, all animals received Carprofen (5 mg/kg body weight; Rimadyl®, Pfizer, Berlin, Germany) immediately, 24, and 48 hours after surgery.

2.4. In vivo PET/CT imaging

In vivo PET/CT imaging was performed 4 and 8 weeks after femoral surgery using a dedicated small animal PET/CT system (nanoScan PET/CT, Mediso, Budapest, Hungary). For each animal, imaging was performed with both 2-[^{18}F]fluoro-2-deoxy-D-glucose ([^{18}F]FDG) and [^{18}F]fluoride, with a delay between first and second radiotracer injection of 24 to 72 h. During PET/CT imaging,

rats were under anesthesia (9–10% desflurane in 0.5 l/min oxygen/air (1:4)). Animals were placed and immobilized prone with their medial axis parallel to axis of the scanner. To maintain optimal resolution, femur defect was positioned in the middle of the transaxial field of view (FOV, 12 × 10 cm). First, CT scan was performed (35 kVp, 980 μmA, voxel size 113 μm) for both anatomic information and attenuation correction of PET data. Second, PET acquisition was started 20 s before intravenous (i.v.) bolus injection of either [^{18}F]FDG or [^{18}F]fluoride (10–20 MBq in 300 μl 0.9% NaCl) through a needle catheter into a lateral tail vein. Emission data were acquired continuously for 60 min. Acquired PET data were sorted into 32 time frames (15 × 10 s, 5 × 30 s, 5 × 60 s, 4 × 300 s, 3 × 600 s) and were reconstructed using Tera-Tomo™ 3D PET reconstruction algorithm (Mediso, Budapest, Hungary).

2.5. Evaluation of PET/CT data

PET/CT data were evaluated using the Rover software, version 3.0.49 (ABX, Radeberg, Germany). PET and CT data were matched by co-registration preprocessing and manual correction, if necessary. First, CT image was rotated so that the femur defect, fixed by the 5-hole plate and 4 screws, can be optimally visualized in all three dimensions (Fig. 1B–E). Afterwards, PET image was rotated using the same parameter settings as for CT. Again, PET and CT data were co-registered and used for further evaluation. Using the fixed threshold method (percent of maximum radiotracer uptake) with manual adjustment, if necessary, volume of interest (VOI) was determined for femur defect ('VOI_{inner}'), femur defect and adjacent tissue ('VOI_{whole}'), and vena cava ('VOI_{blood}'). VOI for healthy bone ('$VOI_{healthy}$') was defined at the contralateral healthy femur. VOI_{blood} was determined in the first minute after radiotracer injection using a mask placed over the middle and lower third of vena cava. VOI_{blood} was defined to be at least 0.1 cm^3 to minimize variations due to low count rates. VOI_{whole}, VOI_{inner}, and $VOI_{healthy}$ were determined at 30–60 min post injection (p.i.). For VOI_{whole} and VOI_{inner}, masks were placed between the two outer and the two inner screws, respectively, enclosing the 5 mm critical size femur defect (Fig. 1D/E).

For all VOIs the mean standardized uptake value (SUV_{mean} = mean activity concentration × weight/injected dose) was computed. A full dynamic evaluation of the PET data was not performed, since a valid arterial input function cannot be derived from the image data due to strong partial volume effects. This mainly affects evaluation of the data measured at early scan time p.i. (i.e. bolus passage), where the image contrast is high. For example, the actual and the measured radiotracer uptake differ by a factor of more than two, even with an optimistic estimate of the spatial image resolution of full width at half maximum (FWHM) = 1.5 mm and a diameter of the vena cava of 2.5 mm, which makes a reliable dynamic evaluation impossible. However, at low image contrast (i.e. at later scan times p.i.) the error is much lower (<10%), which is an acceptable accuracy for computation of the standardized uptake ratio (SUR = target SUV/blood SUV). It was shown that SUR correlates much better with the metabolic uptake rate K_m, derived from Patlak analysis [26], than SUV [27]. Therefore, in the current work we used this parameter as a surrogate parameter for K_m in addition to SUV.

2.6. High-resolution CT and μCT imaging

After 8 weeks, when rats passed all imaging experiments, rats were sacrificed under general anesthesia using CO_2. Femora were resected, soft tissue was removed as far as possible, and plates as well as screws were removed. Femora were put into 4% buffered formaldehyde at 4°C and fixed for at least 3 days. During this time, high-resolution CT imaging (35 kVp, 980 μmA, voxel size 39 μm) using again the dedicated small animal PET/CT system (nanoScan PET/CT, Mediso, Budapest, Hungary) was performed to investigate the remaining femur defect as well as the newly formed (bone) tissue. In addition, μCT imaging (70 kVp, 114 μmA, voxel size 10.5 μm, 200 ms integration time) was carried

out using a vivaCT40 (Scanco Medical AG, Brüttisellen, Switzerland). From μCT data, the bone volume ratio (bone volume (BV)/total volume (TV)) was determined at the femoral mid-diaphysis according to international guidelines [28].

2.7. Histology and Immunohistochemistry

For histological investigation, formalin-fixed femora were decalcified for 21 d with EDTA-based Osteosoft® (Merck, Darmstadt, Germany). Afterwards, specimen were semi-automatically washed, dehydrated, and embedded in paraffin using the Thermo Scientific STP 420ES Tissue Processor (Microm International, Walldorf, Germany). Sequential sections (2 μm) were made in parallel to the longitudinal axis of the femur. Samples were stained with hematoxylin & eosin (H&E; VWR, Darmstadt, Germany) or Weigert's iron hematoxylin & Masson-Goldner staining kit (Gold; #1.00485, Merck, Darmstadt, Germany). For immunohistochemical staining, the specimens were incubated with mouse monoclonal anti-α smooth muscle actin (αSMA; clone 1A4, DAKO, Glostrup, Denmark; 1:750), mouse monoclonal anti-CD68 (clone ED1, Bio-Rad, Feldkirchen, Germany; 1:100), rabbit polyclonal CD163 (LS-C393444, LSBio, Eching, Germany; 1:35), rabbit polyclonal anti-cyclooxygenase-2 (COX-2; ab15191, Abcam, Cambridge, UK; 1:25), or mouse monoclonal anti-transglutaminase-2 (TGase 2; ab2386, Abcam, Cambridge, UK; 1:25). In case of TGase 2, antigen retrieval (sodium citrate buffer, pH 6.0, 12 h, 60°C) had to be performed before. Primary antibodies were detected with the BrightVision Goat Anti-Mouse AP kit (for Act, CD68, and TGase 2; Medac, Wedel, Germany) or the BrightVision Goat Anti-Rabbit AP kit (for CD163 and COX-2; Medac, Wedel, Germany). The immune reaction was visualized by Fast-Red substrate kit (Abcam, Cambridge, UK).

2.8. Statistical analysis

Results are illustrated as mean (bars) + SE with additional presentation of raw data (symbols). Statistical analysis was performed using the Origin 9.1.0G software (OriginLAB, USA). The effects of the GAG coatings were estimated with Bonferroni *post hoc* test (one-way ANOVA). Statistical significance was set at $p < 0.05$.

3. Results

3.1. Clinical findings

All animals survived the surgical procedure and showed no wound infections. Three animals had to be euthanized one day after surgery because of an open wound at the site of surgery (1 × NC, 2 × sHA3). Sixteen animals entered the *in vivo* PET/CT imaging experiments (Table 1; 4 × NC, 4 × Col, 4 × CS, 4 × sHA3). Four animals had to be excluded because of screw loosening (2 × NC, 1 × CS, 1 × sHA3). One animal died because of anesthetic complications during 8 week follow-up [^{18}F]FDG-PET/CT (1 × sHA3).

3.2. Evaluation of PET/CT data

The aim of this pilot study was to assess the feasibility of PET/CT imaging for monitoring of bone healing and tissue regeneration in our rat critical size bone defect model (Fig. 1A). Due to the three-dimensional orientation of femora, rotation of co-registered PET/CT data was a prerequisite for data evaluation. Therefore, PET and CT images were rotated so that the femur defect fixed by the 5-hole

Table 1
Number of animals which underwent surgery and final number of animals per group for data analysis

Surgery	Total number of animals per group							
	NC		Col		CS		sHA3	
	$n=4+1$		$n=4$		$n=4$		$n=4+2$	
	Final number of animals for analysis							
	4 weeks				8 weeks			
	NC	Col	CS	sHA3	NC	Col	CS	sHA3
[^{18}F]Fluoride	$n=2$	$n=4$	$n=3$	$n=3$	$n=2$	$n=4$	$n=3$	$n=3$
[^{18}F]FDG	$n=2$	$n=4$	$n=3$	$n=3$	$n=2$	$n=4$	$n=3$	$n=2$
CT *ex vivo*	n.d.	n.d.	n.d.	n.d.	$n=2$	$n=4$	$n=3$	$n=2$
Histology	n.d.	n.d.	n.d.	n.d.	$n=2$	$n=4$	$n=3$	$n=2$

plate and 4 screws can be optimally visualized in all three dimensions (Fig. 1B–E). This allows for analysis of PET tracer accumulation in the critical size bone defect (red arrow) in comparison to the healthy femur (white arrow) at the contralateral side (Fig. 1B/C). Whereas [^{18}F]FDG predominantly accumulated within the implanted PCL scaffold (Fig. 1B/D), increased accumulation of [^{18}F]fluoride could be observed at the bone defect margins (Fig. 1C/E). To determine the optimal data evaluation strategy, radiotracer uptake was investigated in the two different VOIs defined above (Fig. 1D/E, VOI_{inner} vs. VOI_{whole}). A VOI defined at the contralateral healthy femur ($VOI_{healthy}$) served as control.

3.3. Imaging of cellular glucose consumption by [^{18}F]FDG PET/CT

After i.v. injection of [^{18}F]FDG the radiotracer predominantly accumulated within the PCL scaffolds rather than in adjacent bone tissue. Thereby, elevated [^{18}F]FDG uptake suggests increased cellular glucose consumption, a surrogate for cellular activity, within the aECM-coated PCL scaffolds. By contrast, at the contralateral healthy femur an only low [^{18}F]FDG uptake could be observed (Fig. 1B). Using CT as reference image, [^{18}F]FDG uptake was discriminated between VOI_{whole} and VOI_{inner}. VOI_{whole} was analyzed because analysis of VOI_{inner} may sometimes underestimate [^{18}F]FDG uptake, in the case that PCL scaffold slightly shifted transversal and, therefore, was not anymore located exactly within the defect. Determination of radiotracer uptake in VOI_{whole}, on the other hand, may sometimes overestimate radiotracer accumulation since epiphyses are usually characterized by elevated [^{18}F]FDG uptake (Fig. 1B/D).

Comparative analysis of [^{18}F]FDG accumulation in the critical size femur defect, filled either with no material (NC) or an aECM-coated PCL scaffold, in comparison to the healthy contralateral femur is shown in Fig. 2A-C, whereby [^{18}F]FDG uptake is delineated as SUV_{mean}. Healthy femora showed lowest [^{18}F]FDG accumulation overall. [^{18}F]FDG uptake in NC was slightly elevated, but not significantly different from healthy femoral shaft. Implantation of an aECM-coated PCL scaffold, by contrast, significantly increased [^{18}F]FDG uptake, both after 4 and 8 weeks (Fig. 2A–C). When comparing the different aECM coatings, it became evident that CS-coated PCL scaffolds caused highest [^{18}F]FDG uptake, especially after 4 weeks. After 8 weeks, differences between the various aECM-coated PCL scaffolds diminished. When analyzing VOI_{whole} instead of VOI_{inner} values for NC slightly increased (Fig. 2B/C), probably due to physiological [^{18}F]FDG uptake by epiphyses. Consequently, [^{18}F]FDG uptake in NC became significantly different from healthy femur after 8 weeks and, on the other hand, differences between NC and the aECM-coated PCL scaffolds lost significance (Fig. 2C).

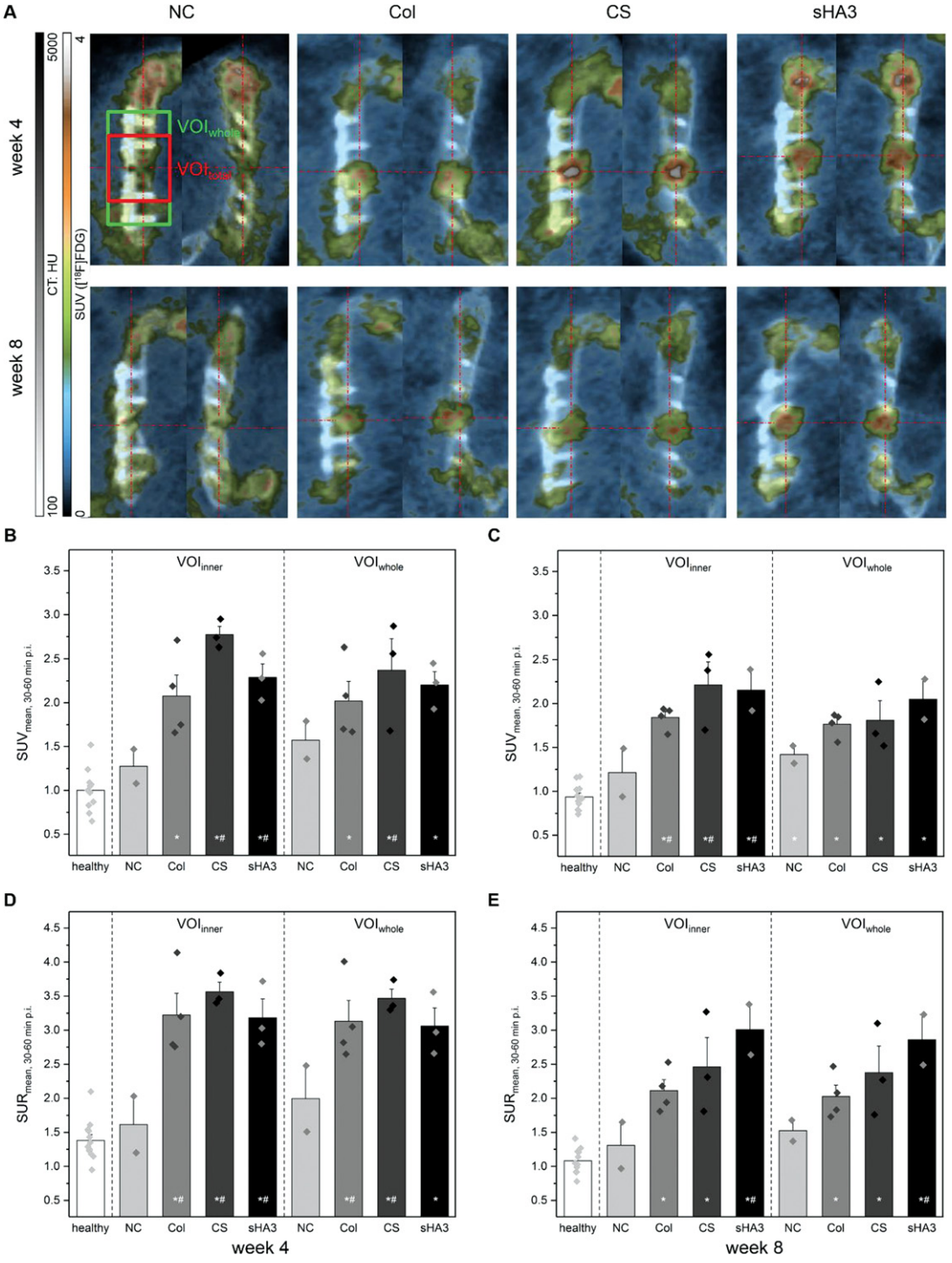

Fig. 2. [^{18}F]FDG accumulation in a rat critical size bone defect implanted with no material (NC) or implanted with PCL scaffolds coated with aECM (Col – collagen, CS – chondroitin sulfate, sHA3 – polysulfated hyaluronan) after 4 and 8 weeks. (A) Representative PET/CT images of [^{18}F]FDG accumulation in rat critical size bone defect after 4 (upper panel) and 8 weeks (lower panel). (B/C) [^{18}F]FDG uptake within determined VOIs calculated as SUV_{mean} at 30–60 min p.i. (D/E) [^{18}F]FDG uptake within determined VOIs calculated as SUR_{mean} at 30–60 min p.i. $^{*}p < 0.05$ vs. $VOI_{healthy}$, $\#p \leq 0.05$ vs. NC.

Since SUR correlates much better with the metabolic uptake rate K_m than SUV, we decided to calculate SUR in addition to SUV as a surrogate parameter for K_m. Contrary to expectations, calculation of SUR does not significantly improve data variation within the groups. However, differences between the groups already observed with SUV approach could be confirmed by analyzing SUR (Fig. 2D/E).

3.4. Imaging of bone mineralization by [^{18}F]fluoride PET/CT

Bone mineralization within the critical size bone defect and adjacent tissue was analyzed by PET/CT imaging after i.v. injection of [^{18}F]fluoride. Again, using CT as reference image, [^{18}F]fluoride uptake for VOI_{whole} and VOI_{inner} was analyzed. VOI_{whole} may better reflect new bone formation in adjacent bone. On the other hand, VOI_{whole} may sometimes overestimate mineralization of newly formed bone, since epiphyses are physiologically characterized by intensive [^{18}F]fluoride accumulation. From representative PET/CT images (Fig. 3A, CS) it became evident, that VOI_{whole} will overestimate new bone formation when the 5-hole plate is eccentrically implanted closer to one of the two epiphysis.

After i.v. injection of [^{18}F]fluoride, highest radiotracer accumulation was observed at the bone defect margins in close proximity to the 5 mm defect, where highest new bone formation and mineralization was expected. When comparing bone defect without PCL scaffold (NC) and the contralateral healthy femur it became evident that there is a significant increase in [^{18}F]fluoride accumulation in the 5 mm critical size bone defect (Fig. 1B, Fig. 3A–C). After 4 weeks, there was a trend to a further increase of [^{18}F]fluoride uptake, when an aECM-coated PCL scaffold was press-fit inserted into the critical size bone defect (Fig. 3B). However, due to small group size and high variation of SUV data this effect did not reach significance. After 8 weeks, bone mineralization rate was the same in NC and aECM-coated PCL scaffolds (Fig. 3C). Again, analysis of SUR instead of SUV did not improve data variation. When comparing VOI_{whole} and VOI_{inner} there was a slight trend towards lower variation of both SUV and SUR values, but the found differences between the different groups were quite the same (Fig. 3B–E).

3.5. High-resolution CT and μCT imaging

After 8 weeks, when rats passed all imaging experiments, explanted femora were analyzed by high-resolution CT and μCT imaging. Before, plate and screws were removed to reduce metal-based CT artefacts. However, this bears the risk to damage the newly formed bone tissue, especially since bone starts to bridge in close proximity to the plate. When bone bridging is still fragile, femora tent to bend, resulting in underestimation of bone volume within the defect area. Therefore, simple scoring of defect closure (Fig. 4B) was preferred over image-based determination of defect volume. However, image-based determination of defect volume was performed for μCT measurements.

After 8 weeks, in none of the rats a full defect closure was achieved (Fig. 4). This finding suggests that the observation period in subsequent studies must be chosen significantly longer. CS- and Col-coated PCL scaffolds showed best defect closure resulting in about 50 % defect bridging, defined as score 3 (Fig. 4A–C). Due to data variability within the groups, scoring gives only an impression. However, results of μCT imaging (Fig. 4D/E) confirmed the results of high resolution CT scoring. Again, CS- and Col-coated PCL scaffolds showed best bone healing after 8 weeks. Bone bridging in sHA3 group, by contrast, seems to be inferior to NC (Fig. 4C/E).

3.6. Histology and Immunohistochemistry

In addition to *in vivo* PET/CT imaging, we investigated in formalin-fixed, paraffin-embedded femur sections various histological/immunohistochemical markers such as hematoxylin and eosin stain (H&E), Masson Goldner trichrome stain (Gold), α smooth muscle actin (αSMA, blood vessels), CD68

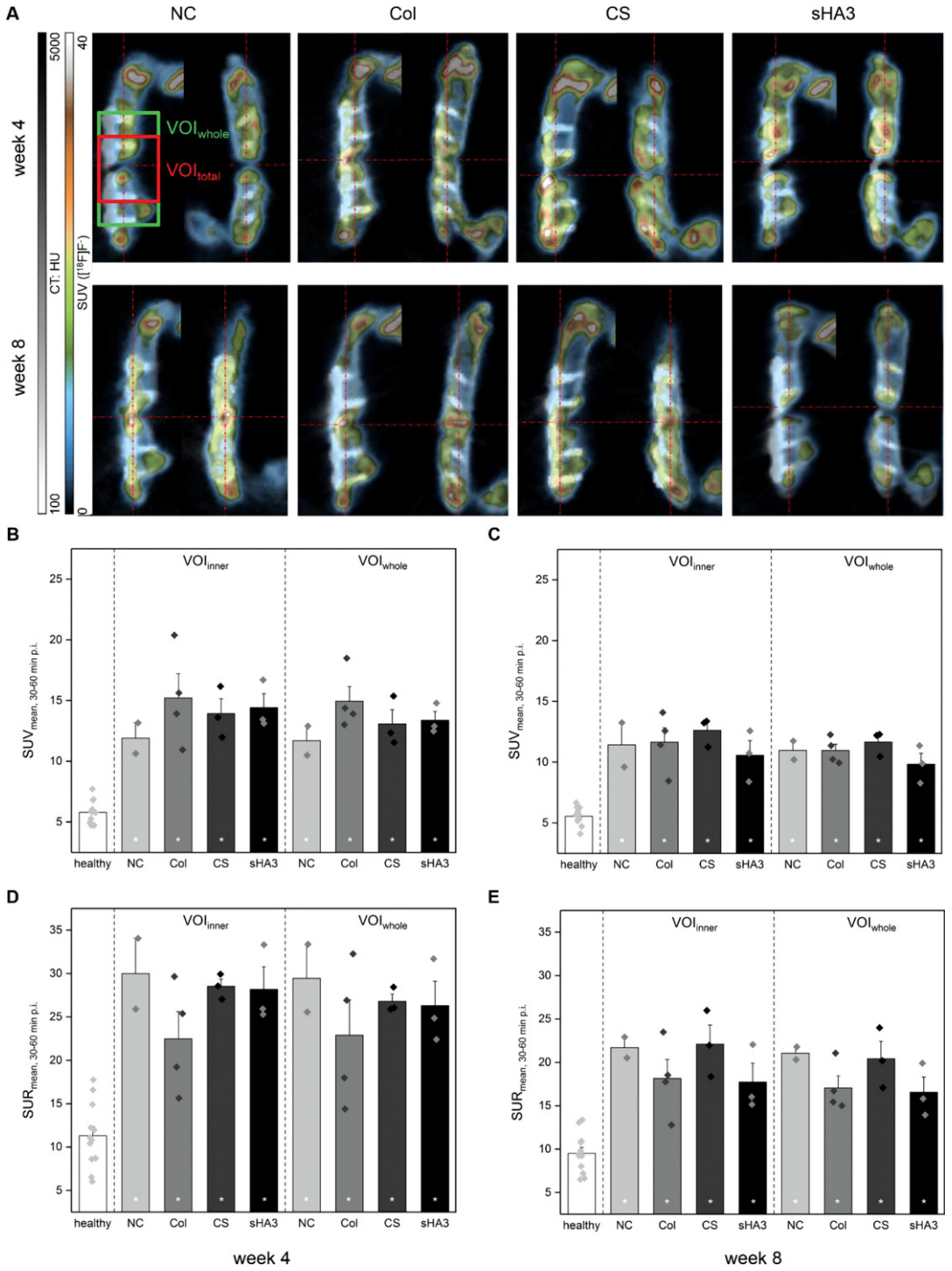

Fig. 3. [^{18}F]fluoride accumulation in a rat critical size bone defect implanted with no material (NC) or implanted with PCL scaffolds coated with different aECM (Col – collagen, CS – chondroitin sulfate, sHA3 – polysulfated hyaluronan) after 4 and 8 weeks. (A) Representative PET/CT images of [^{18}F]fluoride accumulation in rat critical size bone defect after 4 (upper panel) and 8 weeks (lower panel). (B/C) [^{18}F]fluoride uptake within determined VOIs calculated as SUV_{mean} at 30–60 min p.i. (D/E) [^{18}F]FDG uptake within determined VOIs calculated as SUR_{mean} at 30–60 min p.i. $^{*}p \leq 0.05$ vs. $VOI_{healthy}$, $\#p < 0.05$ vs. NC.

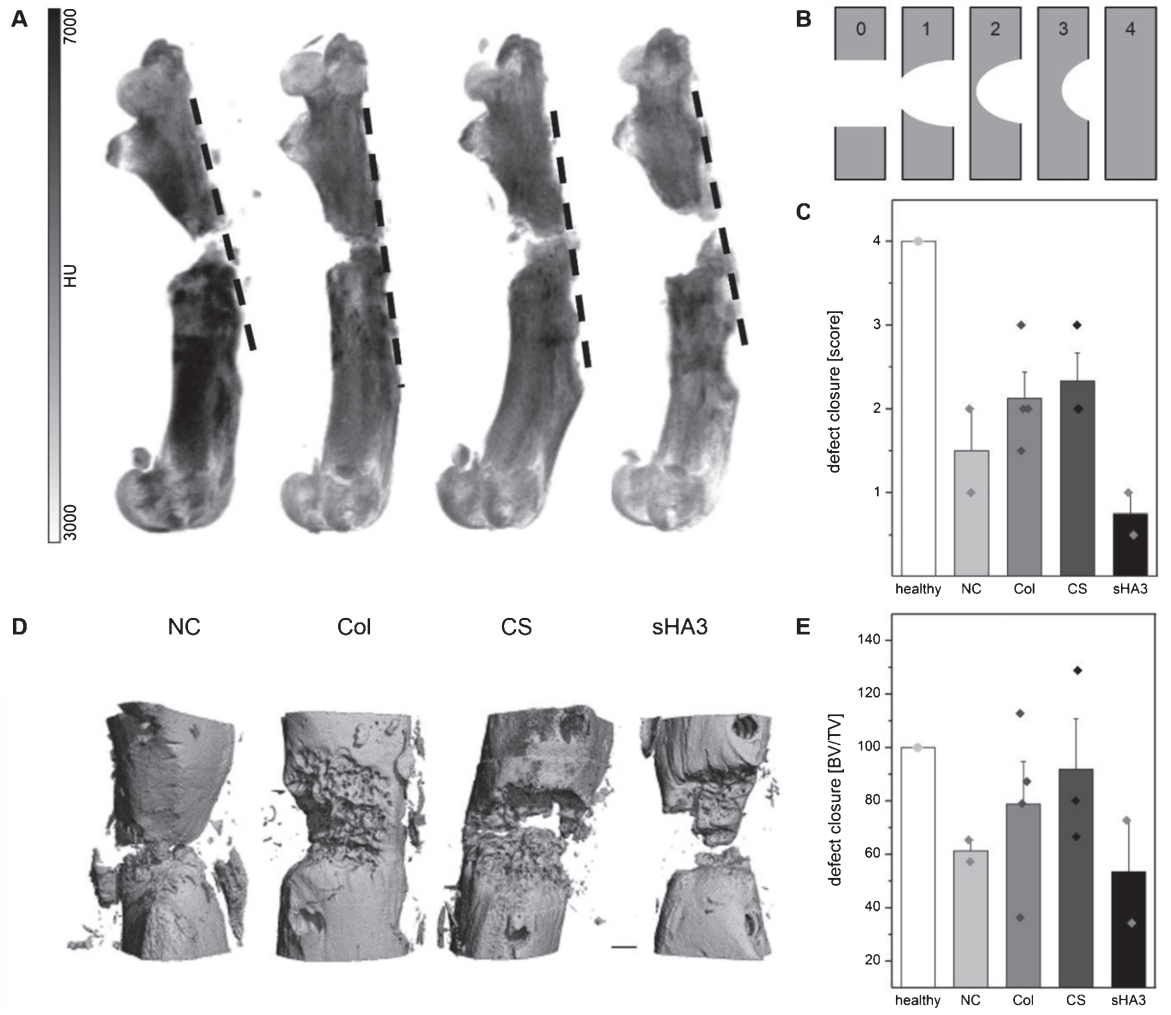

Fig. 4. Analysis of bone bridging in explanted femora 8 weeks after induction of a 5 mm critical size bone defect implanted with no material (NC) or implanted with PCL scaffolds coated with different aECM (Col – collagen, CS – chondroitin sulfate, sHA3 – polysulfated hyaluronan) by CT imaging. (A) Representative high-resolution CT images (voxel size 39 μm). (B) Scoring system to assess bridging of critical size bone defect with 0 = no new bone formation until 4 = full defect closure. (C) Defect closure scores determined from high resolution CT imaging. (D) Representative μCT images (voxel size 10.5 μm); scale bare 1 mm (E) Results of μCT imaging designated as bone volume ratio (bone volume (BV)/ total volume (TV)). $^{*}p \leq 0.05$ vs. $VOI_{healthy}$, $\#p < 0.05$ vs. NC.

(pan-Mϕ), CD163 (M2-Mϕ), cyclooxygenase-2 (COX-2, inflammatory cells), and transglutaminase-2 (TGase 2, ECM remodeling).

Both H&E and Gold stain revealed intense formation of connective tissue/collagen between GAG-coated PCL fibers (white structures) (Fig. 5A–D). Especially for Col- and CS-coated PCL scaffolds there are areas with mature, mineralized bone (Fig. 5B/C, arrow) suggesting promotion of bone formation by Col- and CS-coated PCL scaffolds. By contrast, defect closure in NC (Fig. 5A) appears to be very thin and labile with only fibrous tissue within the defect area. For sHA3-coated scaffolds, especially Gold stain was less intense suggesting less bone formation within 8 weeks (Fig. 5D). Moreover, by contrast to Col- and CS-coated PCL scaffolds the margins between mineralized bone and fibrous

tissue were clearly visible (Fig. 5D, arrow). In all PCL group specimens examined, the new bone was formed by desmal ossification rather than by endochondral bone formation.

By staining of αSMA we investigated vascularization of newly formed (bone) tissue. Even in NC there were several blood vessels, especially in the newly formed tissue (Fig. 5A). Within the aECM-coated PCL scaffolds intense blood vessel formation could be observed, especially in rather non-mineralized bone tissue (Fig. 5E). When newly formed bone tissue reached mature mineralized state there are virtually no blood vessels any more (Fig. 5C, arrow). With regard to the amount of blood vessel formation, Col and sHA3 seem to be slightly superior to CS by trend. However, this effect could also be attributed to the inverse correlation of the amount of blood vasculature and mature bone, since CT imaging revealed highest amount of mature bone in CS group (Fig. 4).

In addition to vascularization, tissue sections were analyzed for the presence of inflammatory cells, e.g. macrophages (pan-Mϕ: CD68, anti-inflammatory M2-Mϕ: CD163) and COX-2 positive cells, including pro-inflammatory M1-Mϕ, chondrocyte progenitors, osteoblasts, and osteoclasts [29–31]. Within the NC we could observe some Mϕ predominantly localized at the bone-new tissue-interphase (Fig. 5A, arrow; Fig. 5F). For all aECM-coated PCL scaffolds, Mϕ could be observed in bone lacunae, in direct contact to the PCL fibers, and, again, at the bone-new tissue-interphase (Fig. 5A–D, Fig. 5G). By contrast to CD68, staining of anti-inflammatory M2-Mϕ was less intense and CD163-positive cells were predominantly located at the bone-new tissue-interphase and in bone marrow (Fig. 5A-D).

Moreover, immunochemical staining revealed involvement of COX-2 (Fig. 5A–D) and TGase 2 (Fig. 5A–D), key enzymes of inflammation and ECM remodelling, respectively, in our model. TGase 2 was predominantly located in bone marrow, around blood vessels (Fig. 5C, arrow), and in close proximity to the aECM coated PCL fibers (Fig. 5H).

4. Discussion

The management of critical size bone defects, caused by trauma, tumor resection or infection still remains a major clinical orthopedic challenge. Implant surface coating with organic components of the extracellular matrix (ECM) creating an artificial ECM (aECM) provides a therapeutic option to generate an osteogenic surface mimicking the native environment for osteogenic cells [13].

The primary objective of this pilot study was to investigate the feasibility of dual-radiotracer PET/CT imaging for the functional characterization of biomaterial-assisted healing of critical size bone defects in the rat model. As a first approach, we used the clinically established radiotracers [^{18}F]FDG and [^{18}F]fluoride to investigate cellular glucose consumption, a surrogate for cellular activation, and bone mineralization, respectively. In this regard, [^{18}F]FDG has already been used to investigate skeletal disorders and new bone formation in patients and a rat femur defect model, respectively [32, 33].

In the present study, a substantial [^{18}F]FDG uptake could be observed within the PCL scaffolds rather than within the adjacent bone tissue. This suggests an intense cell recruitment to and proliferation within the entire PCL scaffolds, a result already found *in vitro* [14, 15]. In this regard, the presence of inflammatory or osteoinductive cells within the PCL scaffold is obvious, but this question has to be addressed with more dedicated radiotracers *in vivo* [34] or immunohistochemistry *ex vivo*. Highest [^{18}F]FDG uptake was observed within the CS-coated PCL scaffolds 4 weeks post surgery, suggesting highest induction of early bone healing processes. With regard to the optimal data evaluation strategy, SUR was not superior to SUV and determination of VOI_{inner} may be more suitable for determination of cellular glucose consumption in the implanted PCL scaffold and adjacent tissue.

Since [^{18}F]fluoride is extracted by the skeletal system in proportion to bone blood flow and osteoblastic activity, [^{18}F]fluoride PET allows for quantification of bone mineralization [35]. As expected, generation of a 5 mm critical size bone defect significantly stimulated new bone formation. However,

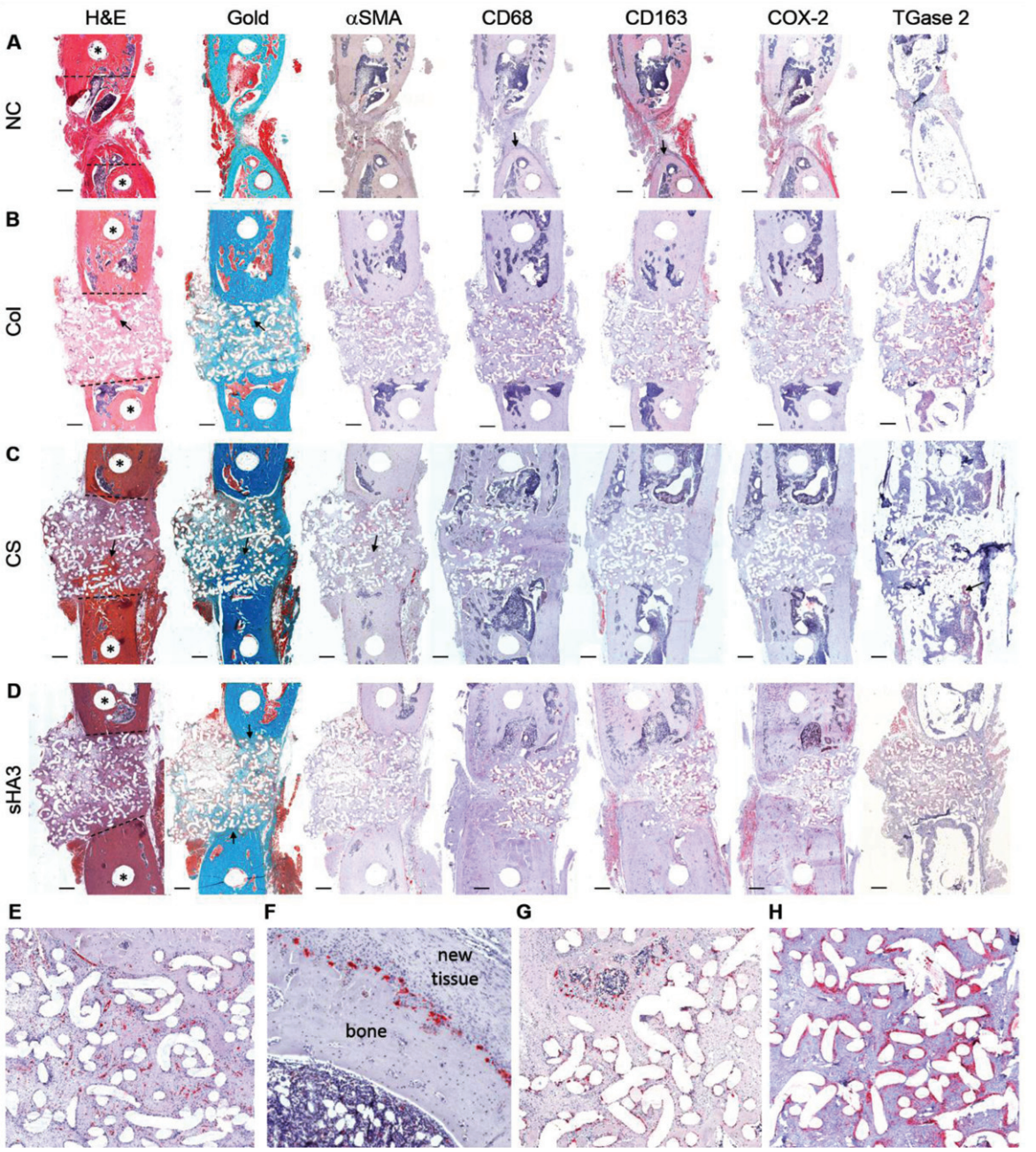

Fig. 5. Histological and immunohistochemical evaluation of 5 mm critical size femur defect implanted with no material (NC) or implanted with PCL scaffolds coated with different GAGs (Col – collagen, CS – chondroitin sulfate, sHA3 – polysulfated hyaluronan) after 8 weeks. (A-D) Representative formalin-fixed paraffin-embedded sections stained with hematoxylin and eosin (H&E), Masson Goldner trichrome (Gold), and specific antibodies against smooth muscle actin (αSMA, blood vessels), CD68 (pan-Mϕ), CD163 (M2-Mϕ), cyclooxygenase-2 (COX-2, inflammatory cells), or transglutaminase-2 (TGase 2, ECM remodeling). *screw hole; scale bare 1 mm (E-H) Representative enlarged sections of staining of αSMA (E), CD68 (F/G), and TGase 2 (H).

further increase of bone mineralization by the implantation of aECM coated PCL scaffolds was only marginal during the observation period. By contrast, previous *in vitro* studies confirmed an increased osteogenic differentiation especially by CS [14]. Again, SUR was not superior to SUV and determination of VOI_{whole} may be more suitable for determination of new bone formation in the critical size defect and adjacent tissue, provided that physiologically increased [^{18}F]fluoride uptake by epiphysis does not interfere with VOI_{whole}.

Animals with osteosythesis failure like screw loosening were characterized by increased radiotracer uptake in the affected regions (data not shown) and, therefore, had to be excluded from data analysis. However, this gives hint that even minimal osteosynthesis failures as well as delayed healing might be identified by PET/CT imaging using clinically established radiotracers. This also suggests that unsuccessful healing can be detected and that early personalized intervention, e.g. through adjuvant therapies, can be considered.

In addition to functional PET imaging, we also investigated newly formed bone volume at 8 weeks post surgery by *ex vivo* CT imaging, as an endpoint marker comparable to our previous studies [13, 15]. In the present study, implantation of CS- or Col-coated PCL scaffolds showed best bone healing, resulting in about 50 % defect bridging. Thereby, our former studies were confirmed, where CS achieved best bone healing both when used as coating of Ti-PEEK plates and PCL scaffolds [13, 15].

As already mentioned, vascularization plays a pivotal role during bone healing [36, 37]. Therefore, the intense formation of blood vessels after implantation of aECM-coated PCL scaffolds is beneficial, since oxygen supply, in addition to biomaterial stiffness, has been shown to favor bone formation [38]. As determined by CD68 and CD163 staining, inflammatory cells, especially Mϕ, are present in the newly formed tissue surrounding and infiltrating aECM-coated PCL scaffolds. In line with this, expression of COX-2, a key enzyme of inflammation [39], could be determined in comparable regions. Presence of inflammatory cells and enzymes is not surprising, since balanced immune response and COX-2/prostaglandin E2 (PGE_2)-pathway appear to be essential for a successful bone healing process [30, 37]. Moreover, we were able to detect TGase 2 in newly formed tissue, especially after implantation of aECM-coated PCL scaffolds, suggesting a role of this enzyme in our model. TGase 2 is a multifunctional enzyme involved in post-translational modification of proteins, (patho) physiological remodeling of ECM, and tissue response to biomaterials [40]. In this regard, increased TGase 2 activity seems to be beneficial for biomaterial-assisted tissue regeneration, since TGase 2 promotes cell-implant interaction, stabilizes implant-tissue interface, and, thereby, improves biocompatibility [41]. Moreover, it has been shown that human osteoblasts show increased spreading on PCL scaffolds when the polymer is coated with TGase 2 and fibronectin [42].

5. Summary and perspective

PET is a highly sensitive and minimally invasive imaging technique which provides quantitative information about the functional expression of individual molecular targets, e.g., inflammatory enzymes, or metabolic processes *in vivo* [43]. This allows conclusions to be drawn, for example, about the active enzyme concentration or receptor density in the healing bone as well as in adjacent tissue. Depending on the research question to be addressed, dedicated radiotracers have to be used or developed [18, 19, 44]. The possibility to use different (radio)tracers and *in vivo* imaging modalities in such an intra-individual setting paves the way to elucidate mechanisms and further influencing factors of biomaterial-assisted bone healing and to characterize them functionally. Moreover, the selection of tracers can be adapted to the different phases of bone healing [45].

With the *in vivo* and *ex vivo* approach presented here, it is already possible to investigate essential hallmarks of the bone healing process. This particularly concerns inflammation and innate

immune response in the early stage, the formation of cartilaginous/osseous callus and its progressing mineralization in the anabolic stage as well as angiogenesis and the formation of secondary bone with regeneration of the original structural features in the catabolic stage. From this, it is possible to derive approaches for the targeted (adjuvant) drug therapy of the various phases and ultimately of bone healing as a whole [2, 46, 47]. For biomaterial research, on the other hand, there are indications for improved modifications and new developments, e.g., in surface coating. With regard to this, biomaterials should not only provide a replacement for the lost bone, but, in addition, should deliver substances, e.g. antibiotics, which address the causative disease of the bone loss [1]. This investigation demonstrated the feasibility of using different PET radiotracers in such an intra-individual setting, revealing at the same time important aspects to be considered. These include time windows for anesthesia sessions, for subsequent tracer application, for combination of radiotracers, taking into account different radionuclides with different half-lives, for the potential application of adjuvant therapeutics, and for the combination of modalities (PET/SPECT, PET/optical imaging, and others). Further points are the use of targeted radiotracers and the required follow-up time. The selected study design can be extended by additional tracers for *in vivo* imaging as well as by markers for final histological characterization to capture further important facets of bone healing processes such as hypoxia, revascularization, and perfusion.

The pilot study presented here essentially served the support of this concept and, finally, the immediate preparation of a multi-arm animal experimental study. In this study, different aECM-coated PCL scaffolds are currently under investigation in the rat model described here. In addition to other clinically established radiotracers, e.g., [^{18}F]fluoromisonidazole ([^{18}F]FMISO) for imaging of hypoxia, experimental radiotracers such as radiolabeled COX-2 inhibitors are applied [18, 48]. In addition, study arms are set up in which the therapeutic influence of biomaterial-assisted bone healing, for example through selective COX-2 inhibitors, is tested [49–51].

Acknowledgments

The authors thank Torsten Kniess, Ph.D., and the staff of the cyclotron and GMP radiopharmaceuticals production units for providing [^{18}F]FDG and [^{18}F]fluoride. The expert technical assistance of Mareike Barth, Helge Gläser, Regina Herrlich, Suzanne Manthey, Sebastian Meister, Aline Morgenegg, Andrea Suhr, Annett Wenke, and Heike Zimmermann also is greatly acknowledged. The authors are thankful to the Deutsche Forschungsgemeinschaft (DFG) for supporting this work within the Collaborative Research Center Transregio 67 “Functional Biomaterials for Controlling Healing Processes in Bone und Skin - From Material Science to Clinical Application“ (CRC/TRR 67/3); project A3 - *Development and characterization of artificial extracellular matrices (aECM) based on collagen and glycosaminoglycan (GAG)-derivatives*, V.H.; project B5 - *In vivo and ex vivo investigation of the effects of artificial matrices on implant surfaces in long bones*, C.N., S.S., Y.F., S.R., & J.P; project Z3 - *Synthesis and allocation of modified glycosaminoglycans (GAG) and artificial extracellular matrices*, S.M., M.S., & D.S). The authors also thank the Helmholtz Association for funding a part of this work through the Helmholtz Cross-Programme Initiative “Technology and Medicine – Adaptive Systems” (C.N., J.W. & J.P.).

Conflict of interest

There is no conflict of interest.

References

[1] Winkler T, Sass FA, Duda GN, Schmidt-Bleek K. A review of biomaterials in bone defect healing, remaining shortcomings and future opportunities for bone tissue engineering: The unsolved challenge. Bone Joint Res. 2018;7(3):232-43.

[2] Rothe R, Schulze S, Neuber C, Hauser S, Rammelt S, Pietzsch J. Adjuvant drug-assisted bone healing: Part I - Modulation of inflammation. Clin Hemorheol Microcirc. 2019;in press (DOI 10.3233/CH-199102).

[3] Roddy E, Debaun MR, Daoud-Gray A, Yang YP, Gardner MJ. Treatment of critical-sized bone defects: Clinical and tissue engineering perspectives. Eur J Orthop Surg Traumatol. 2018;28(3):351-62.

[4] Bauer TW, Muschler GF. Bone graft materials. An overview of the basic science. Clin Orthop Relat Res. 2000;371:10-27.

[5] Willie BM, Petersen A, Schmidt-Bleek K, Cipitria A, Mehta M, Strube P, Lienau J, Wildemann B, Fratzl P, Duda G. Designing biomimetic scaffolds for bone regeneration: Why aim for a copy of mature tissue properties if nature uses a different approach? Soft Matter. 2010;6(20):4976-87.

[6] Bastow ER, Byers S, Golub SB, Clarkin CE, Pitsillides AA, Fosang AJ. Hyaluronan synthesis and degradation in cartilage and bone. Cell Mol Life Sci. 2008;65(3):395-413.

[7] Astachov L, Vago R, Aviv M, Nevo Z. Hyaluronan and mesenchymal stem cells: From germ layer to cartilage and bone. Front Biosci (Landmrk Ed). 2011;16:261-76.

[8] Bierbaum S, Douglas T, Hanke T, Scharnweber D, Tippelt S, Monsees TK, Funk RHW, Worch H. Collageneous matrix coatings on titanium implants modified with decorin and chondroitin sulfate: Characterization and influence on osteoblastic cells. J Biomed Mater Res A. 2006;77a(3):551-62.

[9] Hempel U, Hintze V, Moller S, Schnabelrauch M, Scharnweber D, Dieter P. Artificial extracellular matrices composed of collagen I and sulfated hyaluronan with adsorbed transforming growth factor beta 1 promote collagen synthesis of human mesenchymal stromal cells. Acta Biomater. 2012;8(2):659-66.

[10] Forster Y, Rentsch C, Schneiders W, Bernhardt R, Simon JC, Worch H, Rammelt S. Surface modification of implants in long bone. Biomatter. 2012;2(3):149-57.

[11] Rammelt S, Illert T, Bierbaum S, Scharnweber D, Zwipp H, Schneiders W. Coating of titanium implants with collagen, RGD peptide and chondroitin sulfate. Biomaterials. 2006;27(32):5561-71.

[12] Morra M, Cassinelli C, Cascardo G, Fini M, Giavaresi G, Giardino R. Covalently-linked hyaluronan promotes bone formation around Ti implants in a rabbit model. J Orthop Res. 2009;27(5):657-63.

[13] Förster Y, Bernhardt R, Hintze V, Möller S, Schnabelrauch M, Scharnweber D, Rammelt S. Collagen/glycosaminoglycan coatings enhance new bone formation in a critical size bone defect - A pilot study in rats. Mat Sci Eng C Mater Biol Appl. 2017;71:84-92.

[14] Rentsch B, Hofmann A, Breier A, Rentsch C, Scharnweber D. Embroidered and surface modified polycaprolactone-co-lactide scaffolds as bone substitute: *In vitro* characterization. Ann Biomed Eng. 2009;37(10):2118-28.

[15] Rentsch C, Rentsch B, Breier A, Spekl K, Jung R, Manthey S, Scharnweber D, Zwipp H, Biewener A. Long-bone critical-size defects treated with tissue-engineered polycaprolactone-co-lactide scaffolds: A pilot study on rats. J Biomed Mater Res A. 2010;95a(3):964-72.

[16] Tomihata K, Suzuki M, Oka T, Ikada Y. A new resorbable monofilament stature. Polym Degrad Stabil. 1998;59(1-3):13-18.

[17] Bergmann R, Pietzsch J. Small animal positron emission tomography in food sciences. Amino Acids. 2005;29(4):355-76.

[18] Laube M, Kniess T, Pietzsch J. Radiolabeled COX-2 inhibitors for non-invasive visualization of COX-2 expression and activity - a critical update. Molecules. 2013;18(6):6311-55.

[19] Kniess T, Laube M, Wüst F, Pietzsch J. Technetium-99m based small molecule radiopharmaceuticals and radiotracers targeting inflammation and infection. Dalton Trans. 2017;46(42):14435-51.

[20] Cheng C, Alt V, Pan L, Thormann U, Schnettler R, Strauss LG, Heinemann S, Schumacher M, Gelinsky M, Nies B, Dimitrakopoulou-Strauss A. Application of F-18-sodium fluoride (NaF) dynamic PET-CT (dPET-CT) for defect healing: A comparison of biomaterials in an experimental osteoporotic rat model. Med Sci Monit. 2014;20:1942-9.

[21] Cheng C, Alt V, Pan L, Thormann U, Schnettler R, Strauss LG, Schumacher M, Gelinsky M, Dimitrakopoulou-Strauss A. Preliminary evaluation of different biomaterials for defect healing in an experimental osteoporotic rat model with dynamic PET-CT (dPET-CT) using F-18-sodium fluoride (NaF). Injury. 2014;45(3):501-5.

[22] Rother S, Salbach-Hirsch J, Moeller S, Seemann T, Schnabelrauch M, Hofbauer LC, Hintze V, Scharnweber D. Bioinspired collagen/glycosaminoglycan-based cellular microenvironments for tuning osteoclastogenesis. ACS Appl Mater Interfaces. 2015;7(42):23787-97.

[23] Kalbitzer L, Franke K, Moller S, Schnabelrauch M, Pompe T. Glycosaminoglycan functionalization of mechanically and topologically defined collagen I matrices. J Mater Chem B. 2015;3(45):8902-10.

[24] Hintze V, Moeller S, Schnabelrauch M, Bierbaum S, Viola M, Worch H, Scharnweber D. Modifications of hyaluronan influence the interaction with human bone morphogenetic protein-4 (hBMP-4). Biomacromolecules. 2009;10(12):3290-7.
[25] Kunze R, Rosler M, Moller S, Schnabelrauch M, Riemer T, Hempel U, Dieter P. Sulfated hyaluronan derivatives reduce the proliferation rate of primary rat calvarial osteoblasts. Glycoconj J. 2010;27(1):151-8.
[26] Patlak CS, Blasberg RG. Graphical evaluation of blood-to-brain transfer constants from multiple-time uptake data - generalizations. J Cerebr Blood F Met. 1985;5(4):584-90.
[27] van den Hoff J, Oehme L, Schramm G, Maus J, Lougovski A, Petr J, Beuthien-Baumann B, Hofheinz F. The PET-derived tumor-to-blood standard uptake ratio (SUR) is superior to tumor SUV as a surrogate parameter of the metabolic rate of FDG. EJNMMI Res. 2013;3(1):77.
[28] Bouxsein ML, Boyd SK, Christiansen BA, Guldberg RE, Jepsen KJ, Muller R. Guidelines for assessment of bone microstructure in rodents using micro-computed tomography. J Bone Miner Res. 2010;25(7):1468-86.
[29] Lu LY, Loi F, Nathan K, Lin TH, Pajarinen J, Gibon E, Nabeshima A, Cordova L, Jamsen E, Yao Z, Goodman SB. Pro-inflammatory M1 macrophages promote Osteogenesis by mesenchymal stem cells via the COX-2-prostaglandin E2 pathway. J Orthop Res. 2017;35(11):2378-85.
[30] Naik AA, Xie C, Zuscik MJ, Kingsley P, Schwarz EM, Awad H, Guldberg R, Drissi H, Puzas JE, Boyce B, Zhang X, O'keefe RJ. Reduced COX-2 expression in aged mice is associated with impaired fracture healing. J Bone Miner Res. 2009;24(2):251-64.
[31] Lin HN, O'connor JP. Immunohistochemical localization of key arachidonic acid metabolism enzymes during fracture healing in mice. PLoS One. 2014;9(2):e88423.
[32] Cheng C, Alt V, Dimitrakopoulou-Strauss A, Pan L, Thormann U, Schnettler R, Weber K, Strauss LG. Evaluation of new bone formation in normal and osteoporotic rats with a 3-mm femur defect: Functional assessment with dynamic PET-CT (dPET-CT) using 2-deoxy-2-[(18)F]fluoro-D-glucose (18)F-FDG and (18)F-fluoride. Mol Imaging Biol. 2013;15(3):336-44.
[33] Guhlmann A, Brecht-Krauss D, Sugar G, Glatting G, Kotzerke J, Kinzl L, Reske SN. Chronic osteomyelitis: Detection with FDG PET and correlation with histopathologic findings. Radiology. 1998;206(3):749-54.
[34] Wu C, Li F, Niu G, Chen X. PET imaging of inflammation biomarkers. Theranostics. 2013;3(7):448-66.
[35] Hawkins RA, Choi Y, Huang SC, Hoh CK, Dahlbom M, Schiepers C, Satyamurthy N, Barrio JR, Phelps ME. Evaluation of the skeletal kinetics of fluorine-18-fluoride ion with PET. J Nucl Med. 1992;33(5):633-42.
[36] Schell H, Duda GN, Peters A, Tsitsilonis S, Johnson KA, Schmidt-Bleek K. The haematoma and its role in bone healing. J Exp Orthop. 2017;4(1):5.
[37] Schmidt-Bleek K, Petersen A, Dienelt A, Schwarz C, Duda GN. Initiation and early control of tissue regeneration - bone healing as a model system for tissue regeneration. Expert Opin Biol Ther. 2014;14(2):247-59.
[38] Burke DP, Kelly DJ. Substrate stiffness and oxygen as regulators of stem cell differentiation during skeletal tissue regeneration: A mechanobiological model. Plos One. 2012;7(7):e40737.
[39] Simmons DL, Botting RM, Hla T. Cyclooxygenase isozymes: The biology of prostaglandin synthesis and inhibition. Pharmacol Rev. 2004;56(3):387-437.
[40] Pietsch M, Wodtke R, Pietzsch J, Loser R. Tissue transglutaminase: An emerging target for therapy and imaging. Bioorg Med Chem Lett. 2013;23(24):6528-43.
[41] Hakimzadeh N, Stewart DJ, Courtman DW. The role of transglutaminase 2 and osteopontin in matrix protein supplemented microencapsulation of marrow stromal cells. Biomaterials. 2010;31(35):9256-65.
[42] Heath DJ, Christian P, Griffin M. Involvement of tissue transglutaminase in the stabilisation of biomaterial/tissue interfaces important in medical devices. Biomaterials. 2002;23(6):1519-26.
[43] Van Den Hoff J. Principles of quantitative positron emission tomography. Amino Acids. 2005;29(4):341-53.
[44] Kniess T. Radiolabeled small molecule inhibitors of VEGFR - recent advances. Curr Pharm Des. 2012;18(20):2867-74.
[45] Einhorn TA, Gerstenfeld LC. Fracture healing: Mechanisms and interventions. Nat Rev Rheumatol. 2015;11(1):45-54.
[46] Rothe R, Schulze S, Neuber C, Hauser S, Rammelt S, Pietzsch J. Adjuvant drug-assisted bone healing: Part II - Modulation of angiogenesis. Clin Hemorheol Microcirc. 2019; in press (DOI 10.3233/CH-199103).
[47] Rothe R, Schulze S, Neuber C, Hauser S, Rammelt S, Pietzsch J. Adjuvant drug-assisted bone healing: Part III - Further strategies for local and systemic modulation. Clin Hemorheol Microcirc 2019; in press (DOI 10.3233/CH-199104).
[48] Kniess T, Laube M, Bergmann R, Sehn F, Graf F, Steinbach J, Wuest F, Pietzsch J. Radiosynthesis of a F-18-labeled 2,3-diarylsubstituted indole via McMurry coupling for functional characterization of cyclooxygenase-2 (COX-2) *in vitro* and *in vivo*. Bioorg Med Chem. 2012;20(11):3410-21.
[49] Bechmann N, Kniess T, Kockerling M, Pigorsch A, Steinbach J, Pietzsch J. Novel (pyrazolyl)benzenesulfonamides with a nitric oxide-releasing moiety as selective cyclooxygenase-2 inhibitors. Bioorg Med Chem Lett. 2015;25(16):3295-3300.

[50] Roscales S, Bechmann N, Weiss DH, Kockerling M, Pietzsch J, Kniess T. Correction: Novel valdecoxib derivatives by ruthenium(ii)-promoted 1,3-dipolar cycloaddition of nitrile oxides with alkynes - synthesis and COX-2 inhibition activity. MedChemComm. 2018;9(3):591-2.

[51] Laube M, Gassner C, Sharma SK, Gunther R, Pigorsch A, König J, Köckerling M, Wuest F, Pietzsch J, Kniese T. Diaryl-substituted (dihydro)pyrrolo[3,2,1-hi]indoles, a class of potent COX-2 inhibitors with tricyclic core structure. J Org Chem. 2015;80(11):5611-24.